Preprints.org

Article

Not peer-reviewed version

Sensorless Capability Expansion for SPMSM based on Inductance Parameter Identification

Peng Chen *, Ruiqing Ma , Zhe Chen

Posted Date: 27 May 2024

doi: 10.20944/preprints202405.1675.v1

Keywords: sensorless capability; inductance parameter identification; saliency ratio; convergence region; heavy load status; SPMSM

Preprints.org is a free multidiscipline platform providing preprint service that is dedicated to making early versions of research outputs permanently available and citable. Preprints posted at Preprints.org appear in Web of Science, Crossref, Google Scholar, Scilit, Europe PMC.

Copyright: This is an open access article distributed under the Creative Commons Attribution License which permits unrestricted use, distribution, and reproduction in any medium, provided the original work is properly cited.

Preprints.org (www.preprints.org) | NOT PEER-REVIEWED | Posted: 27 May 2024 doi:10.20944/preprints202405.1675.v1

Disclaimer/Publisher's Note: The statements, opinions, and data contained in all publications are solely those of the individual author(s) and contributor(s) and not of MDPI and/or the editor(s). MDPI and/or the editor(s) disclaim responsibility for any injury to people or property resulting from any ideas, methods, instructions, or products referred to in the content.

Article

Sensorless Capability Expansion for SPMSM Based on Inductance Parameter Identification

Peng Chen *, Ruiqing Ma and Zhe Chen

School of Automation, Northwestern Polytechnical University, Xi'an, China
* Correspondence: cooper_chenpeng@163.com

Abstract: Pulsating high frequency voltage injection can be used for sensorless control of SPMSM at zero and low speed ranges. However, the sensorless capability still faces challenges to the requirements of industrial application, especially at heavy load status. Aiming at this issue, this article proposes a sensorless capability expansion method for SPMSM based on inductance parameter identification. First, incremental inductances at *d*-*q*-axis and cross-coupling inductance are identified by three steps combining the rotating high frequency voltage injection and pulsating high frequency voltage injection, then, using polynomial curve fitting algorithm, apparent inductances are calculated. Second, positive DC current injection at *d*-axis is proposed to enhance the saliency ratio based on the analysis of parameter identification results. Compared with the conventional $i_d=0$ or $i_d<0$ method, when positive DC current is injected at *d*-axis, saliency ratio is enhanced. Third, convergence region is expanded at heavy load status and accuracy of rotor position estimation is improved using the proposed method. Finally, the experiment results validate that the sensorless capability of SPMSM is expanded.

Keywords: sensorless capability; inductance parameter identification; saliency ratio; convergence region; heavy load status; SPMSM

1. Introduction

Permanent magnet synchronous motors (PMSMs) are widely used for industry applications due to the high-power density, high-torque density and high-efficiency. Sensorless control of PMSM is hot topic of research in recent decades [1]. Once the position sensor is removed, the cost is reduced. Meanwhile, the reliability is improved because the additional cables are not needed any more.

Sensorless control methods for PMSM can be divided into two categories. The first category is model-based method. When the motor is operating at medium and high-speed ranges, rotor position can be estimated by the back electromotive force (EMF) [2]. The second category is saliency-based method [3]. By injecting high frequency (HF) voltage into the motor, the saliency effect can be used for rotor position estimation at zero and low speed ranges.

Among the three typical HF voltage injection methods, the accuracy of position estimation is low for the rotating high frequency voltage injection method [4]; The phase delay is small for the high frequency square wave voltage injection method. However, high switching frequency leads to high noise and high loss [5]; Compared with the two methods above, pulsating high frequency voltage injection method has the advantages of high accuracy and good stability [6], it has been gradually promoted for industrial applications.

Although pulsating high frequency voltage injection method can be used for sensorless control of SPMSM, Sensorless capability still faces challenges to the requirements of the actual application. It is very necessary to invest the limitation of the saliency based senorless control method [7–10]. Sensorless capability are comprised of saliency ratio, estimation error, and convergence region [7,8]. When pulsating high frequency voltage injection is used for sensorless control of SPMSM, it is found that as load increases, the saliency ratio decreases due to the saturation effect, the convergence region of sensorless control is limited. Sensorless control method even fails at severe status. Meanwhile, due

© 2024 by the author(s). Distributed under a Creative Commons CC BY license.

Preprints.org (www.preprints.org) | NOT PEER-REVIEWED | Posted: 27 May 2024 doi:10.20944/preprints202405.1675.v1

to the cross-coupling effect, the estimated rotor position gradually deviates from the actual rotor position, the accuracy of position estimation is degraded [9,10]. Therefore, research on sensorless capability expansion for SPMSM at heavy load status is of great value.

In order to expand the sensorless capability for PMSM based on saliency effect, a lot of researches have been carried out. The two main categories are motor body design optimization and motor control improvement. In the first category, motor design method is proposed to achieve self-sensing capability while retaining the torque-speed capability for PMSM used in a hybrid electric vehicle [11]. By adding a short-circuited rotor-ring into the two-pole slotless permanent-magnet motor, the saliency ratio is expanded to 1.8 [12]. An improved inductance model is proposed to reduce the torque ripple and enhance the self-sensing capabilities of TC-PMSMs [13]. In the second category, using the current reference tilting strategy [14,15], the rotor position estimation error is reduced and the torque limitation is expended. In [16], a new online method is proposed to detect and compensate the position estimation error due to the cross-coupling effect, the accuracy of position estimation is improved.

Apart from the methods above, it is noticed that inductance parameter identification is an effective way to invest the sensorless capability of PMSM based on saliency effect [17]. The two kinds of inductances in the voltage equation of PMSM are incremental inductance and apparent inductance. In [18,19], finite element analysis method is used for incremental inductance parameters identification. However, the method is limited at the motor design process. In [20], driving the motor operating at a constant speed, flux linkage versus current curve of the machine is constructed, then, incremental inductances are identified using partial differentiation calculation. In [21], when the rotor position is locked, rotor speed term in the voltage equation is ignored, incremental inductances are identified based on the simplified the fundamental voltage equation. However, the common issue in [20,21] is that the computation of partial differentiation is large. High frequency voltage injection is proposed for incremental inductances identification in [22,23]. However, cross-coupling inductance is ignored. In [24], incremental inductance and cross-coupling inductance are identified using rotating high frequency voltage injection method. In [25,26], with the assistant of position sensor, high frequency voltages are injection into the actual reference frame, the position observer is removed, the incremental inductance identification process is easy and the accuracy can be guaranteed. Besides the incremental inductances, apparent inductances are also important parameters in motor drive technical. In [20,21], apparent inductances are identified according to the flux linkage versus current curve of PMSM. However, the inductance identification fails when the fundamental current is zero. In [27,28], polynomial curve fitting algorithm is proposed for apparent inductance identification. Comparing with the method in [20,21], the apparent inductances can be calculated even the fundamental current is zero.

According to the analysis above, this article proposes a sensorless capability expansion method for SPMSM based on inductance parameter identification. The incremental inductances at *d*-*q*-axis and cross-coupling inductance are identified combining the rotating high-frequency voltage injection and pulsating high-frequency voltage injection method. Then, sixth order polynomial curve fitting algorithm is proposed for apparent inductance identification. Based on the inductance identification results, positive DC current injection at *d*-axis is proposed to expand the sensorless capability of SPMSM. Finally, the effectiveness of the proposed method is verified using a 200W SPMSM.

2. Conventional Pulsating High Frequency Voltage Injection

2.1. Incremental Inductance and Apparent Inductance

The voltage equation considering cross-coupling effect involves multiple inductance parameters.

Among them, incremental inductance is known as dynamic inductance, transient inductance, differential inductance, etc. Incremental inductance represents the slope at the operating point on the flux linkage-current curve, which is commonly used for small signal model analysis. For example, PI parameter tuning of the current loop, inductance calculation in high-frequency injection method, etc.

Preprints.org (www.preprints.org) | NOT PEER-REVIEWED | Posted: 27 May 2024 doi:10.20944/preprints202405.1675.v1

Apparent inductance, also known as static inductance, absolute inductance, etc. It represents the ratio of magnetic flux to current. The inductance in the torque equation is apparent inductance. Figure 1 shows the difference between the incremental and apparent inductance. Under no-load conditions, incremental inductance is almost equal to apparent inductance. However, as load increases, due to the saturation effect, the incremental inductance is gradually less than the apparent inductance.

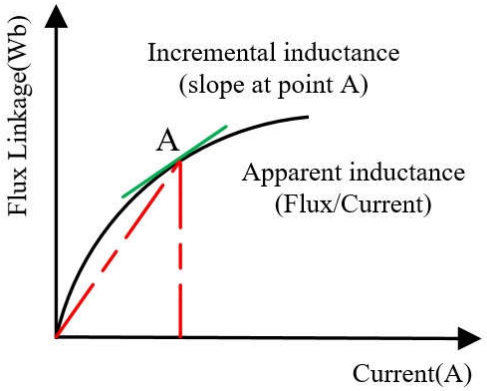

Figure 1. Incremental inductance and apparent inductance.

2.2. Conventional Pulsating High Frequency Voltage Injeciton Method

The voltage equation of PMSM at *d*-*q*-axis is shown as

$$\begin{aligned} u_d &= i_d R + L_d^{inc}\frac{di_d}{dt} + L_{dq}^{inc}\frac{di_q}{dt} - \omega_e L_q^{app} i_q \\ U_q &= i_q R + L_q^{inc}\frac{di_q}{dt} + L_{qd}^{inc}\frac{di_d}{dt} + \omega_e (L_d^{app} i_d + \psi_{PM}) \end{aligned} \tag{1}$$

where, u_d, u_q, i_d, i_q, are the voltages and currents at *d*-*q*-axis, R is the phase resistance, ω_e is the rotor speed, L_d^{inc}, L_q^{inc} are incremental inductance at *d*-*q*-axis, $L_{dq}^{inc}, L_{qd}^{inc}$ are the incremental cross-coupling inductance between *d*-*q*-axis and their values are equal. L_d^{app}, L_q^{app} are apparent inductances at *d*-*q*-axis. ψ_{PM} is PM flux linkage.

Considering that the frequency of the voltage injected is much higher than the fundamental frequency and the motor is operating at zero and low speed range, the voltage drop of the resistance and the speed related term in equation (1) can be ignored. The HF model of PMSM is shown as

$$\begin{bmatrix} u_{dh} \\ u_{qh} \end{bmatrix} = \begin{bmatrix} L_d^{inc} & L_{dq}^{inc} \\ L_{dq}^{inc} & L_q^{inc} \end{bmatrix} \begin{bmatrix} \frac{di_{dh}}{dt} \\ \frac{di_{qh}}{dt} \end{bmatrix} \tag{2}$$

where, $u_{dh}, u_{qh}, i_{dh}, i_{qh}$, are the HF voltages and currents at *d*-*q*-axis.

For pulsating high frequency voltage injection method, the HF voltage is injected into the estimated *d*-axis

$$\begin{bmatrix} \hat{u}_{dh} \\ \hat{u}_{qh} \end{bmatrix} = \begin{bmatrix} U_h \cos \omega_h t \\ 0 \end{bmatrix} \tag{3}$$

where $\hat{u}_{dh}, \hat{u}_{qh}$ are the HF voltages at the estimated *d*-*q*-axis, U_h, ω_h are the amplitude and frequency of the injected voltage.

Preprints.org (www.preprints.org) | NOT PEER-REVIEWED | Posted: 27 May 2024 doi:10.20944/preprints202405.1675.v1

The rotor position and reference frames in HF voltage injection method are shown as Figure 2. Where $\alpha\beta$ is the stationary reference frame, dq is the actual synchronous rotating reference frame, $\hat{d}\hat{q}$ is the estimated synchronous rotating reference frame, θ is the actual rotor position, $\hat{\theta}$ is the estimated rotor position, $\Delta\theta$ is the difference between the actual rotor position and the estimated rotor position.

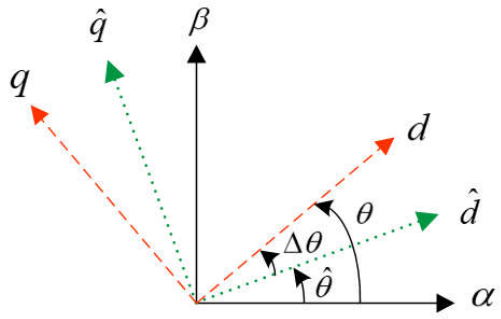

Figure 2. Reference frame and rotor position estimation.

By coordinate transformation, voltage equation at the estimated d-q-axis can be obtained as:

$$\begin{bmatrix}\hat{u}_{dh}\\ \hat{u}_{qh}\end{bmatrix}=\begin{bmatrix}\Sigma_L-\Delta_L\cos 2\Delta\theta-L_{dqh}\sin 2\Delta\theta & -\Delta_L\sin 2\Delta\theta+L_{dqh}\cos 2\Delta\theta\\ -\Delta_L\sin 2\Delta\theta+L_{dqh}\cos 2\Delta\theta & \Sigma_L+\Delta_L\cos 2\Delta\theta+L_{dqh}\sin 2\Delta\theta\end{bmatrix}p\begin{bmatrix}\hat{i}_{dh}\\ \hat{i}_{qh}\end{bmatrix} \tag{4}$$

where $\Sigma_L=\dfrac{L_q^{inc}+L_d^{inc}}{2}$, $\Delta_L=\dfrac{L_q^{inc}-L_d^{inc}}{2}$, $L_{dqh}=L_{dq}^{inc}$, $\hat{i}_{dh},\hat{i}_{qh}$ are HF current at the estimated d-q-axis.

Substitute (3) to (4), the HF current response is expressed as

$$\begin{bmatrix}\hat{i}_{dh}\\ \hat{i}_{qh}\end{bmatrix}=\frac{U_h\sin\omega_h t}{\omega_h(\Sigma_L^2-\Delta_L^2-L_{dqh}^2)}\begin{bmatrix}\Sigma_L+\sqrt{\Delta_L^2+L_{dqh}^2}\cos(2\Delta\theta-\theta_m)\\ \sqrt{\Delta_L^2+L_{dqh}^2}\sin(2\Delta\theta-\theta_m)\end{bmatrix} \tag{5}$$

where θ_m is the cross-coupling angle, $\tan(\theta_m)=L_{dqh}/\Delta_L$。

It is observed that rotor position is contained in the current response of q-axis. So, it can be used for position estimation.

Using bandpass filter to extract the HF current response at the estimated q-axis. then, multiplying with $\sin\omega_h t$, the doubling frequency component is eliminated using a lowpass filter. The remained part for rotor position information is shown as

$$\hat{i}_{qh}=\frac{U_h\sqrt{\Delta_L^2+L_{dqh}^2}}{\omega_h(\Sigma_L^2-\Delta_L^2-L_{dqh}^2)}\sin(2\Delta\theta-\theta_m) \tag{6}$$

Using (6) as the input of PLL based position observer, the rotor position can be estimated when (6) is converged to zero at steady status. It is noticed that additional estimation error is occurred duo the cross-coupling effect.

$$\Delta\theta=\frac{1}{2}\theta_m\approx\frac{1}{2}\tan^{-1}\left(\frac{L_{dqh}}{\Delta_L}\right) \tag{7}$$

In the conventional pulsating high frequency voltage injection method, the cross-coupling effect is always ignored. The error signal for position estimation is expressed as

Preprints.org (www.preprints.org) | NOT PEER-REVIEWED | Posted: 27 May 2024 doi:10.20944/preprints202405.1675.v1

$$\hat{i}_{qh} = \frac{U_h \Delta L}{\omega_h (\Sigma_L^2 - \Delta_L^2)} \sin(2\Delta\theta) \tag{8}$$

The control block of the conventional pulsating high frequency voltage injection is shown as Figure 3.

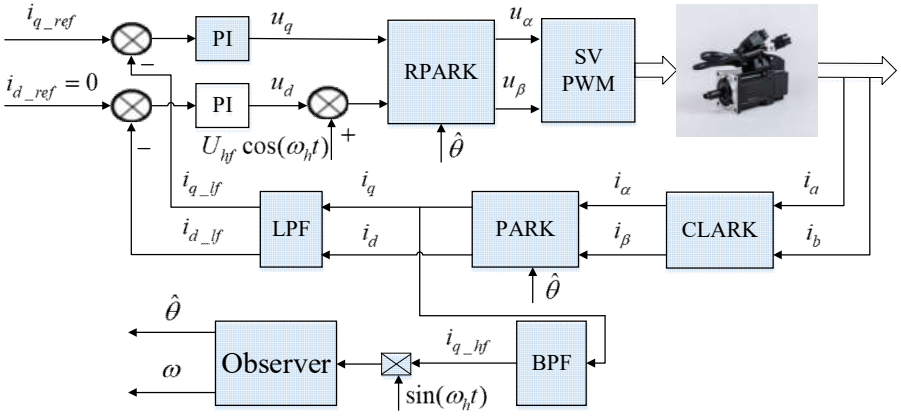

Figure 3. Conventional pulsating high frequency voltage injection method.

2.3. Issues of the Conventional Pulsating High Frequency Voltage Injeciton Method

Although pulsating high frequency voltage injection can be used for sensorless control of SPMSM, the sensorless capability still faces challenges for actual application:

- Saliency ratio is weak and it decreases with the increasing of load. There is no structure saliency for SPMSM, the saturation saliency is weak even HF voltage is injected. Saliency ratio may less than 1 when the motor is operating at heavy load status.
- Convergence region is limited and sensorless control method even diverges at serious situation. [1,9] pointed out that it is very necessary to invest the convergence range for the sensorless control of PMSM, make sure the guaranteed stable sensorless performance is achieved.
- Accuracy of position estimation is degraded due to the cross-coupling effect. Lots of research are carried out to compensate the estimation error due to cross-coupling effect. However, cross-coupling inductance is small and it varies with the increasing of load, the identification of cross-coupling inductance is not easy.

3. The Proposed Sensorless Capability Expansion Method

Aiming to solve the issues above, sensorless capability expansion method for SPMSM is proposed based on Inductance parameter identification in this section.

3.1. Inductance Parameter Identification

3.1.1. Incremental Inductance Identification

It is found that inductance information is contained in the amplitude of HF current response when HF voltage is injected into the motor. So, it can be used for inductance parameter identification.

In this section, the incremental inductances at *d*-*q*-axis and cross-coupling inductance are identified by three steps combining the rotating high frequency voltage injection and pulsating high frequency voltage injection [25,26].

Step 1: positive and negative sequency component of HF current extraction by injecting HF voltage at $\alpha\beta$-axis.

HF voltage injected at $\alpha\beta$-axis is shown as

Preprints.org (www.preprints.org) | NOT PEER-REVIEWED | Posted: 27 May 2024 doi:10.20944/preprints202405.1675.v1

$$\begin{bmatrix} u_{\alpha h} \\ u_{\beta h} \end{bmatrix} = \begin{bmatrix} U_h \cos \omega_h t \\ U_h \sin \omega_h t \end{bmatrix} \tag{9}$$

The voltage equation at $\alpha\beta$-axis is expressed as

$$\begin{bmatrix} u_{\alpha h} \\ u_{\beta h} \end{bmatrix} = \begin{bmatrix} \Sigma_L - \Delta_L \cos 2\theta - L_{dqh} \sin 2\theta & -\Delta_L \sin 2\theta + L_{dqh} \cos 2\theta \\ -\Delta_L \sin 2\theta + L_{dqh} \cos 2\theta & \Sigma_L + \Delta_L \cos 2\theta + L_{dqh} \sin 2\theta \end{bmatrix} p \begin{bmatrix} i_{\alpha h} \\ i_{\beta h} \end{bmatrix} \tag{10}$$

Substitute (9) into (10), the HF current response is shown as

$$\begin{bmatrix} i_{\alpha h} \\ i_{\beta h} \end{bmatrix} = \frac{U_h}{\omega_h (\Sigma_L^2 - \Delta_L^2 - L_{dqh}^2)} \begin{bmatrix} \Sigma_L \sin \omega_h t + \Delta_L \sin(\omega_h t - 2\theta) + L_{dqh} \cos(\omega_h t - 2\theta) \\ -\Sigma_L \cos \omega_h t + \Delta_L \cos(\omega_h t - 2\theta) - L_{dqh} \sin(\omega_h t - 2\theta) \end{bmatrix} \tag{11}$$

The vector expression of (11) is

$$i_{\alpha\beta h} = I_p e^{j(\omega_h t - \frac{\pi}{2})} + I_n e^{j(\frac{\pi}{2} + 2\theta - \omega_h t - \theta_m)} \tag{12}$$

where

$$I_p = \frac{U_h \Sigma_L}{\omega_h (\Sigma_L^2 - \Delta_L^2 - L_{dqh}^2)} \tag{13}$$

$$I_n = \frac{U_h \sqrt{\Delta_L^2 + L_{dqh}^2}}{\omega_h (\Sigma_L^2 - \Delta_L^2 - L_{dqh}^2)} \tag{14}$$

It shows that amplitude of the positive and negative sequence component contains incremental inductance information. they can be used for incremental inductance identification. However, (13) and (14) are not enough to identify the three parameters of incremental inductance.

Step 2: HF current extraction by injecting HF voltage at *d*-axis

HF voltage injected at *d*-axis is shown as

$$\begin{bmatrix} u_{dh} \\ u_{qh} \end{bmatrix} = \begin{bmatrix} U_h \cos \omega_h t \\ 0 \end{bmatrix} \tag{15}$$

The current response is expressed as

$$\begin{bmatrix} i_{dh} \\ i_{qh} \end{bmatrix} = \frac{U_h \sin \omega_h t}{\omega_h (\Sigma_L^2 - \Delta_L^2 - L_{dqh}^2)} \begin{bmatrix} \Sigma_L + \sqrt{\Delta_L^2 + L_{dqh}^2} \cos(2\Delta\theta - \theta_m) \\ \sqrt{\Delta_L^2 + L_{dqh}^2} \sin(2\Delta\theta - \theta_m) \end{bmatrix} \tag{16}$$

Because the HF voltage is injected at the actual *d*-axis, $\Delta\theta$ is zero. Sine and cosine values of the cross-coupling angle are calculated according to (7). Then, amplitude of HF current at *d*-*q*-axis can be deduced as:

$$I_{d1} = \frac{U_h (\Sigma_L + \Delta_L)}{\omega_h (\Sigma_L^2 - \Delta_L^2 - L_{dqh}^2)} \tag{17}$$

$$I_{q1} = \frac{U_h (-L_{dqh})}{\omega_h (\Sigma_L^2 - \Delta_L^2 - L_{dqh}^2)} \tag{18}$$

Step 3: HF current extraction by injecting HF voltage at *q*-axis

Preprints.org (www.preprints.org) | NOT PEER-REVIEWED | Posted: 27 May 2024 doi:10.20944/preprints202405.1675.v1

$$\begin{bmatrix} u_{dh} \\ u_{qh} \end{bmatrix} = \begin{bmatrix} 0 \\ U_h \cos \omega_h t \end{bmatrix} \tag{19}$$

The HF current response is expressed as

$$\begin{bmatrix} i_{dh} \\ i_{qh} \end{bmatrix} = \frac{U_h \sin \omega t}{\omega_h (\Sigma_L^2 - \Delta_L^2 - L_{dqh}^2)} \begin{bmatrix} \sqrt{\Delta_L^2 + L_{dqh}^2} \sin(2\Delta\theta - \theta_m) \\ \Sigma_L - \sqrt{\Delta_L^2 + L_{dqh}^2} \cos(2\Delta\theta - \theta_m) \end{bmatrix} \tag{20}$$

Similar to (15-16), when HF voltage is injected at the actual q-axis, amplitude of HF current at d-q-axis can be deduced as

$$I_{d2} = \frac{U_h(-L_{dqh})}{\omega_h(\Sigma_L^2 - \Delta_L^2 - L_{dqh}^2)} \tag{21}$$

$$I_{q2} = \frac{U_h(\Sigma_L - \Delta_L)}{\omega_h(\Sigma_L^2 - \Delta_L^2 - L_{dqh}^2)} \tag{22}$$

Finally, combining (13,14,17,18,21,22), d-q-axis incremental inductances and cross-coupling inductance can be identified, shown as

$$L_d^{inc} = \frac{2U_h I_p I_{q2}}{\omega_h (I_p^2 - I_n^2)(I_{d1} + I_{q2})} \tag{23}$$

$$L_q^{inc} = \frac{2U_h I_p I_{d1}}{\omega_h (I_p^2 - I_n^2)(I_{d1} + I_{q2})} \tag{24}$$

$$L_{dqh} = -\frac{U_h I_{q1} \text{ or } I_{d2}}{\omega_h (I_p^2 - I_n^2)} \tag{25}$$

3.1.2. Apparent Inductance Identification

Apart from incremental inductances, apparent inductances are also important parameters for identification.

In this section, sixth-order polynomial curve fitting algorithm is proposed for apparent inductance identification base on the incremental inductance identification results.

The incremental inductance matrix considering cross-coupling effect is a non-diagonal matrix, which includes the cross-coupling inductance. Therefore, it is necessary to transform the non-diagonal inductance matrix into a diagonal inductance matrix. Then, it will be easier to use the polynomial curve fitting algorithm for apparent inductance identification.

Using the matrix transformation, diagonal inductance matrix can be obtained as

$$L_{dq\_adj}^{inc} = T(\theta_m) \begin{bmatrix} L_d^{inc} & L_{dqh} \\ L_{dqh} & L_q^{inc} \end{bmatrix} T^{-1}(\theta_m) = \begin{bmatrix} L_{d\_adj}^{inc} & 0 \\ 0 & L_{q\_adj}^{inc} \end{bmatrix} \tag{26}$$

where, $L_{d\_adj}^{inc}$ and $L_{q\_adj}^{inc}$ are the incremental inductances after transformation.

The matrix used for transformation is defined as

$$T(\theta_m) = \begin{bmatrix} \cos\theta_m & -\sin\theta_m \\ \sin\theta_m & \cos\theta_m \end{bmatrix} \tag{27}$$

After transformation, the incremental inductance is diagonal matrix, sixth-order polynomial curve fitting algorithm is proposed as

Preprints.org (www.preprints.org) | NOT PEER-REVIEWED | Posted: 27 May 2024 doi:10.20944/preprints202405.1675.v1

$$L_{d\_adj}^{inc} = m_6 i_d^6 + m_5 i_d^5 + m_4 i_d^4 + m_3 i_d^3 + m_2 i_d^2 + m_1 i_d + m_0 \tag{28}$$

$$L_{q\_adj}^{inc} = n_6 i_q^6 + n_5 i_q^5 + n_4 i_q^4 + n_3 i_q^3 + n_2 i_q^2 + n_1 i_q + n_0 \tag{29}$$

Using the tool of "nlinfit" of MATLAB, the co-efficient of (25) and (26) can be obtained. Then, apparent inductance can be identified as:

$$L_d^{app} = \frac{\int L_{dd\_adj}^{inc} di_d}{i_d} = \frac{1}{7} m_5 i_d^6 + \frac{1}{6} m_5 i_d^5 + \frac{1}{5} m_4 i_d^4 + \frac{1}{4} m_3 i_d^3 + \frac{1}{3} m_2 i_d^2 + \frac{1}{2} m_1 i_d + m_0 \tag{30}$$

$$L_q^{app} = \frac{\int L_{qq\_adj}^{inc} di_q}{i_q} = \frac{1}{7} n_6 i_q^6 + \frac{1}{6} n_5 i_q^5 + \frac{1}{5} n_4 i_q^4 + \frac{1}{4} n_3 i_q^3 + \frac{1}{3} n_2 i_q^2 + \frac{1}{2} n_1 i_q + n_0 \tag{31}$$

3.2. Sensorless Capability Expansion

Figure 4 shows the proposed sensorless capability expansion method in this paper.

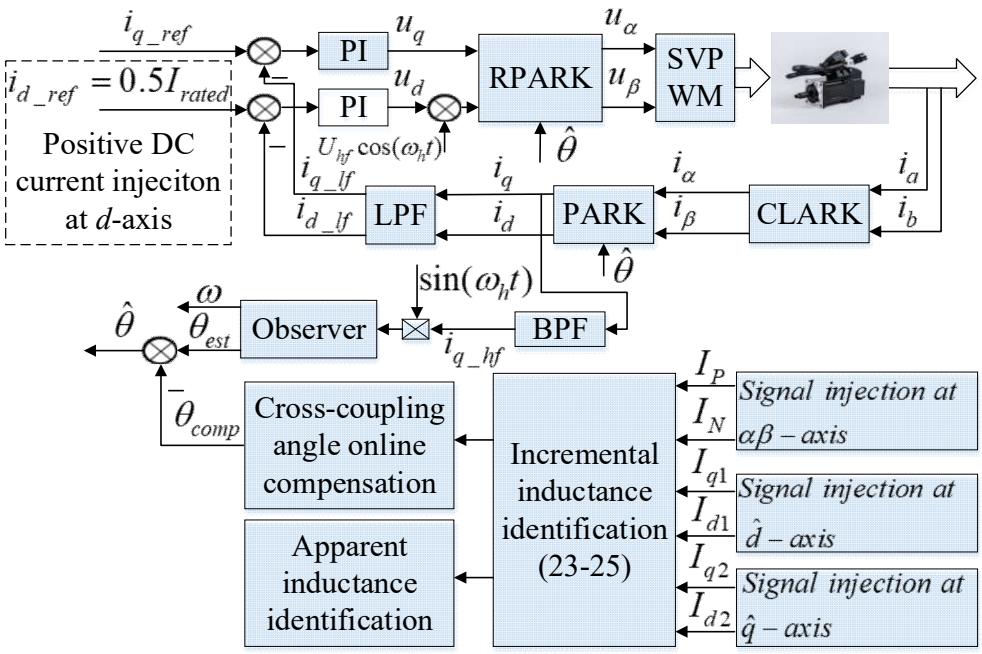

Figure 4. The proposed sensorless capability expansion method for SPMSM.

On one hand, combining the rotating and pulsating high frequency voltage injection method, incremental inductances and cross-coupling inductance are identified. Then, sixth-order polynomial curve fitting algorithm is proposed for apparent inductance identification base on the incremental inductance identification results. On the other hand, according to the inductance parameter identification results, it is found that compared with the conventional $i_d = 0$ or $i_d < 0$ method, the saliency ratio is enhanced obviously when positive DC current is injected into d-axis. However, positive i_d would generate additional copper losses, the efficiency is reduced. After balancing the saliency ratio improvement and efficiency reduction, 50% rated current injection at d-axis is proposed in this paper. The saliency ratio is enhanced, the convergence region is expanded. Meanwhile, the accuracy of position estimation is improved when the estimation error due to the cross-coupling effect is compensated online.

Preprints.org (www.preprints.org) | NOT PEER-REVIEWED | Posted: 27 May 2024 doi:10.20944/preprints202405.1675.v1

$$\hat{\theta} = \theta_{est} - \theta_{comp} \tag{32}$$

where $\hat{\theta}$ is the estimated position after compensation, θ_{est} is position estimated by the observer, θ_{comp} is the compensated angle ,which is equal to $-0.5\theta_m$.

4. Experimental Verification

4.1. Experimental Platform

Parameters of SPMSM used in the paper are listed in Table 1.

Table 1. Parameters of the test motor.

Item	Value	Item	Value
Rated voltage	110 V	Pole pairs	5
Rated current	1.5 A	Phase resistance	2.8 Ω
Rated power	200 W	*d*-axis inductance	13 mH
Rated torque	0.64 Nm	*d*-axis inductance	13 mH

The experimental platform is shown in Figure 5. The MCU in the drive is selected as STM32F405, the resolution of the AD converter is 12 bits, PWM switching frequency is 20kHz, and the dead time is 800ns. During the experiment, two identical drivers were used to control two identical SPMSMs. Among them, the tested motor operates in current loop mode, the load motor operates in speed loop mode, and the two drivers are connected to the power supply through a common DC bus. In order to compare the estimated rotor position accuracy, the encoder of 2500 line resolution was used to obtain the actual rotor position. Software in PC is developed based on the VISA function of LabVIEW, the baud rate is 500kbit/s.

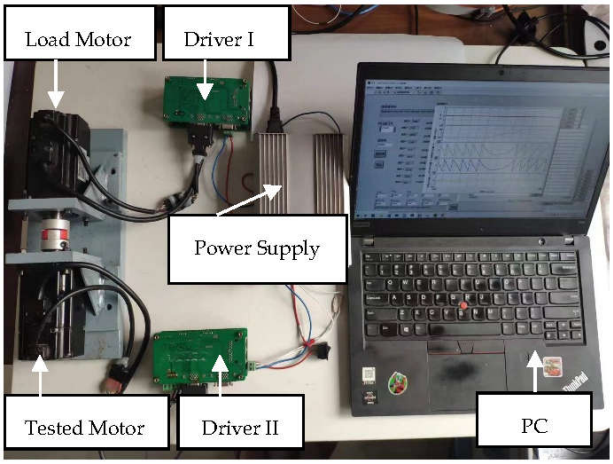

Figure 5. Experiment platform.

4.2. Inductance Papameters Indetification

4.2.1. Incremental Inductance Identification

Figure 6 shows the incremental inductance parameter identification results.

Preprints.org (www.preprints.org) | NOT PEER-REVIEWED | Posted: 27 May 2024 doi:10.20944/preprints202405.1675.v1

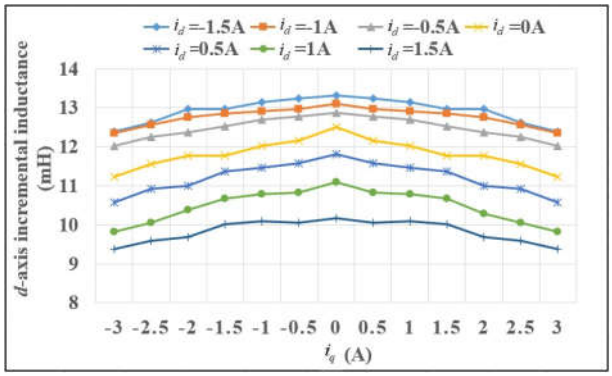

(a)

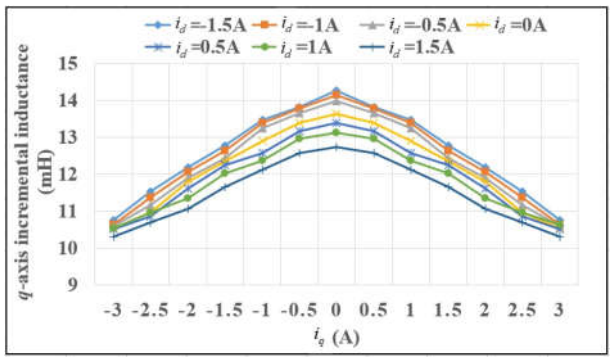

(b)

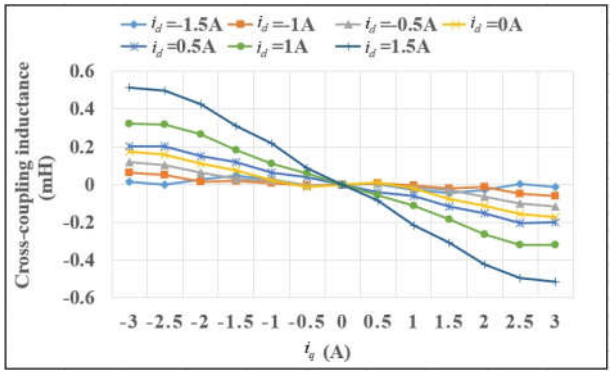

(c)

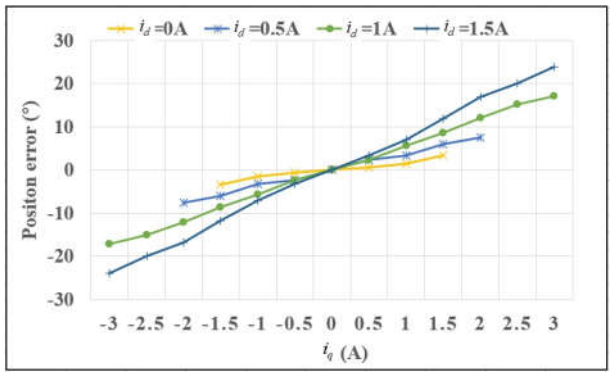

(d)

Figure 6. Incremental inductances identification. (a) L_d^{inc}; (b) L_q^{inc}; (c) L_{dqh}; (d) $-0.5\theta_m$.

Preprints.org (www.preprints.org) | NOT PEER-REVIEWED | Posted: 27 May 2024 doi:10.20944/preprints202405.1675.v1

The frequency and amplitude selection of the HF voltage injected is critical for incremental inductance identification. The higher the frequency is, the greater amplitude is

needed, resulting in higher HF losses. Therefore, the frequency of the voltage injected cannot be too high. At the same time, in order to reduce the nonlinearity of the inverter, the amplitude of the voltage injected should be as large as possible. However, if the amplitude of the HF voltage is too large, saturation of the magnetic field will be increased and the resolution of the incremental inductance is reduced. Therefore, amplitude of the injected signal also needs to be selected appropriately. Finally, after comparing the parameter identification results of 100Hz, 300Hz, 500HZ, 300Hz/26V is selected for incremental inductance identification in this section.

In order to know how the incremental inductances are affected by i_d and i_q, in the experiment, i_d is set as 0, ±0.5A, ±1A, ±1.5A; i_q is set as 0, ±0.5A, ±1A, ±1.5A, ±2A, ±2.5A, ±3A, respectively. Therefore, 91 test points and 7 curves are included in each figure.

As shown in Figures 6a,b, it can be seen that due to the saturation and cross-coupling effect, the incremental inductance of L_d^{inc} and L_q^{inc} gradually decreases with the increase of i_q, the variation of L_q^{inc} is more significant than that of L_d^{inc}. This will lead to the decrease of the saliency ratio. Figure 6c shows the identification results of L_{dqh}. Take the curve $i_d = 1.5A$ as example, it is observed that cross-coupling inductance is -0.358mH when i_q = 1.5A and it reaches -0.515mH when i_q = 3A, which is 200% rated current. It means that the cross-coupling effect increases with the load. Figure 6d shows the calculated rotor position error due to the cross-coupling effect, which is equal to -0.5 θ_m. It can be seen that the estimation error of rotor position increases with the load. Therefore, compensation is needed to improve the accuracy of position estimation, especially at heavy load status.

4.2.2. Apparent Inductance Identification

Apart from incremental inductance identification, apparent inductances are also key parameters for the motor drive. The tool of "nlinfit" in MATLAB is used for apparent inductance identification in this section.

Figure 7a shows apparent inductance identification results of L_d^{app} when $i_q = 0$. It can be seen that L_d^{app} is 12.97 mH when $i_d = -1.5A$. With the increase of i_d, apparent inductance L_d^{app} decreases to 11.45 mH when $i_d = 1.5A$. Figure 7b shows identification results of L_q^{app} when $i_d = 0$. It can be seen that L_q^{app} decreases with the increase of i_q. L_q^{app} decreases to 12.41mH when $i_q = 3A$, which is 200% rated load. Compared with the method in [20,21], apparent inductance can be identified even the fundamental current is zero using the proposed polynomial curve fitting algorithm.

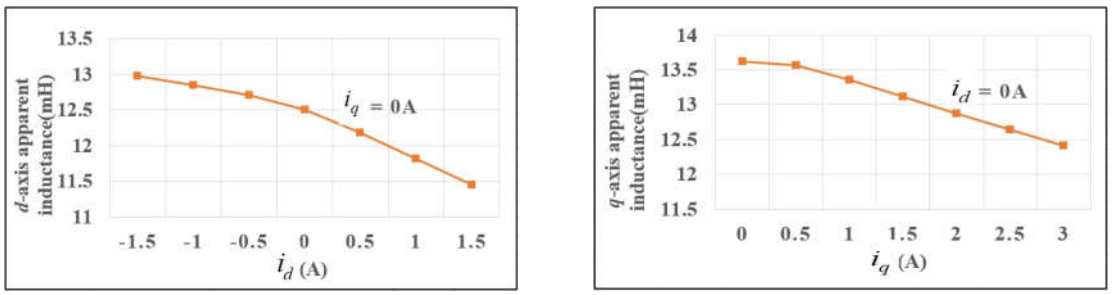

(a) (b)

Figure 7. Apparent inductance identification result. (a) L_d^{app} ;(b) L_q^{app}.

Preprints.org (www.preprints.org) | NOT PEER-REVIEWED | Posted: 27 May 2024 doi:10.20944/preprints202405.1675.v1

4.3. Sensorless Capability Expansion Performance

4.3.1. Saliency Ratio Improvement

Based on incremental inductance identification results, saliency ratio L_q^{inc} / L_d^{inc} at different working point is shown as Figure 8.

The following features can be observed from Figure 8.

- Saliency ratio decreases as i_q increases. This is because L_q^{inc} is more sensitive than L_d^{inc} to the variation of i_q. Saliency ratio is less than 1 at severe cases.
- Saliency ratio can be enhanced when positive DC current is injected into *d*-axis. Take $i_q = 2A$ (130% rated current) as example, using the conventional $i_d < 0$ or $i_d = 0$ method, Saliency ratio is less than 1, it can be predicted that the HF voltage injection method would fail at these situations. On the contrary, saliency ratio gradually increases with the positive value of i_d. Saliency ratio reaches 1.13 when $i_d = 1.5A$.

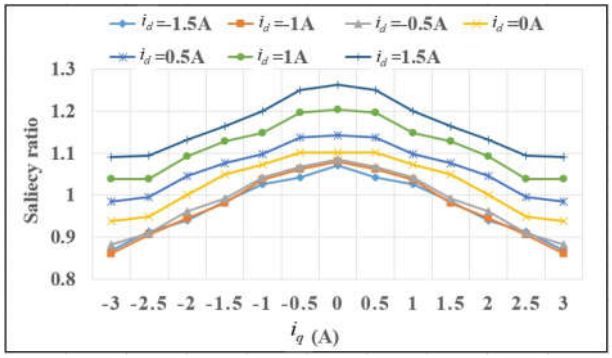

Figure 8. The variation of saliency ratio.

According to the analysis above, it can be predicted that using the proposed method, when 50% rated current is injected at *d*-axis, saliency ratio would be enhanced, comparing with the conventional $i_d = 0$ or $i_d < 0$ method.

4.3.2. Convergence Region Expansion

In the following section, i_d,i_q, actual rotor speed, estimated rotor speed, actual rotor position, estimated rotor position, position error are listed in each figure.

Figure 9 compares the convergence range of the sensorless control between the conventional method and the proposed method at 120r/min.

As shown in Figure 9a, the sensorless control method fails at 130% rated load. This is because the saliency ratio is less 1 at this working point. The experiment result is consistent with the analysis of Figure 8. In Figure 9b, using the proposed method, it is observed that sensorless control method works well at 130% rated load, furthermore, the convergence range is even expanded to 200% rated load. It is also observed the estimated rotor position gradually deviates from the actual rotor position due to the crossing coupling effect. Nearly 12° DC bias error is occurred at 200% rated load. In Figure 9c, using the online compensation method, the DC bias error is eliminated, rotor position error keeps around at 0° regardless the increasing of the load. Figure 9 verifies that the convergence region of the sensorlsess control is expanded to 200% rated load using the proposed method.

Preprints.org (www.preprints.org) | NOT PEER-REVIEWED | Posted: 27 May 2024 doi:10.20944/preprints202405.1675.v1

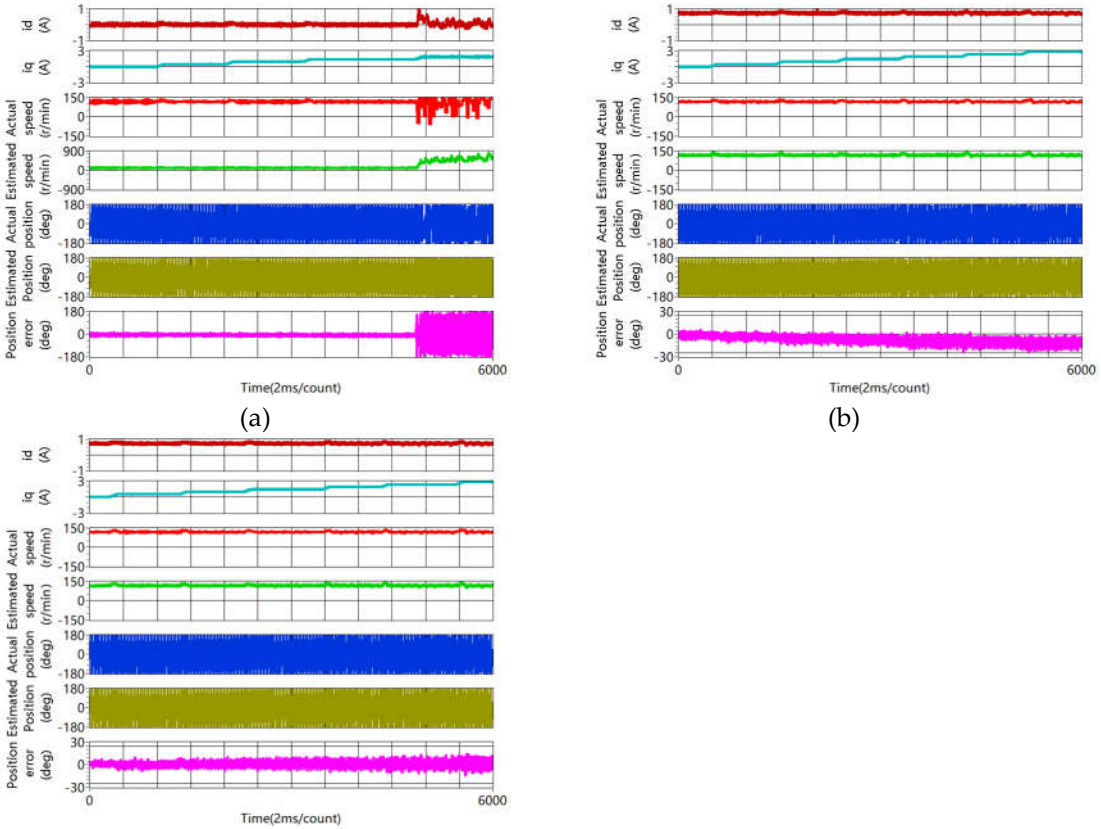

Figure 9. Experiment results of convergence range comparison at 120r/min. (a) Conventional method; (b) Proposed method without compensation for the position estimation error due to cross-coupling effect. (c) Proposed method with compensation for the position estimation error due to cross-coupling effect.

4.3.3. Accuracy of Rotor Position Estimation Improvement

In order to verify how the accuracy of rotor position estimation is improved using the proposed method, the following experiments are carried out.

Figure 10 shows the comparison of the startup performance between the conventional method and the proposed method with rated load. As shown in Figure 10a, it can be seen the motor can start from 0 to 120r/min using the conventional method, however, position error increases with rotor speed, the maximum error exceeds 20 ° at steady status. On the contrary, using the proposed method, position error is less than ±10° during the startup process. Meanwhile, the speed estimation is smoother. It proves that the startup performance is better using the proposed method.

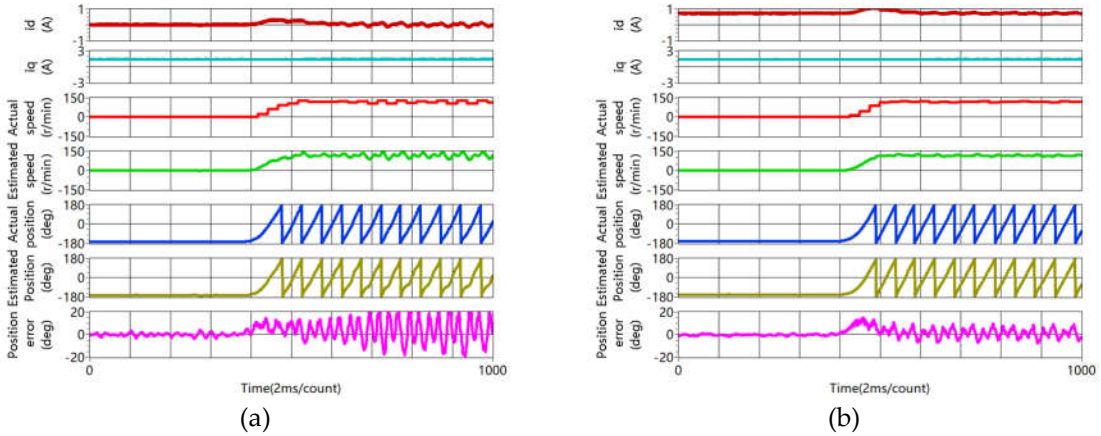

Preprints.org (www.preprints.org) | NOT PEER-REVIEWED | Posted: 27 May 2024 doi:10.20944/preprints202405.1675.v1

Figure 10. Comparison of rotor position estimation during starting process (from 0 to 120 r/min with rated load). (a) Conventional method; (b) Proposed method.

Figure 11 shows the experiment results of rotor position estimation when the motor is operating at 120r/min with rated load. As shown in Figure 11a, using the conventional $i_d = 0$ method, the position estimation error is greater than $\pm 20°$. However, as shown in Figure 12b, using the proposed method, the estimation error keeps within $\pm 10°$ at steady status. it proves the accuracy of rotor position estimation is improved obviously using the proposed method.

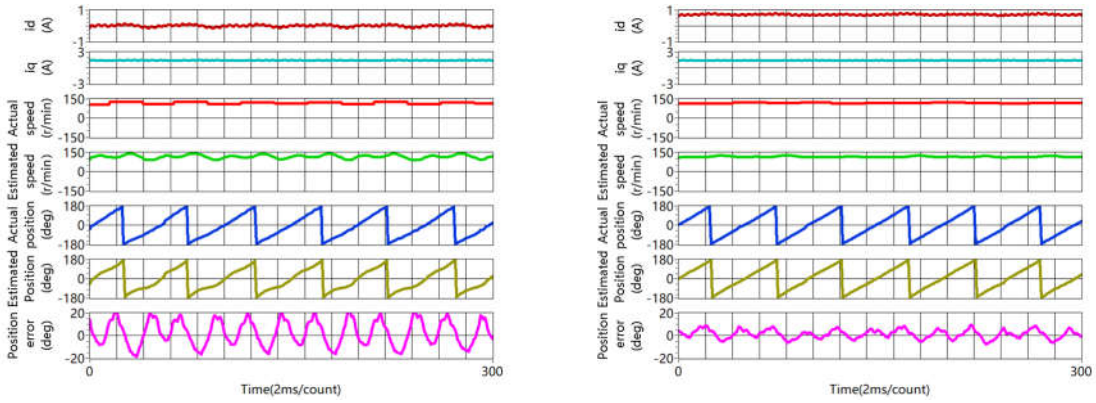

Figure 11. Rotor position estimation at 120r/min with rated load. (a) Conventional method; (b) Proposed method.

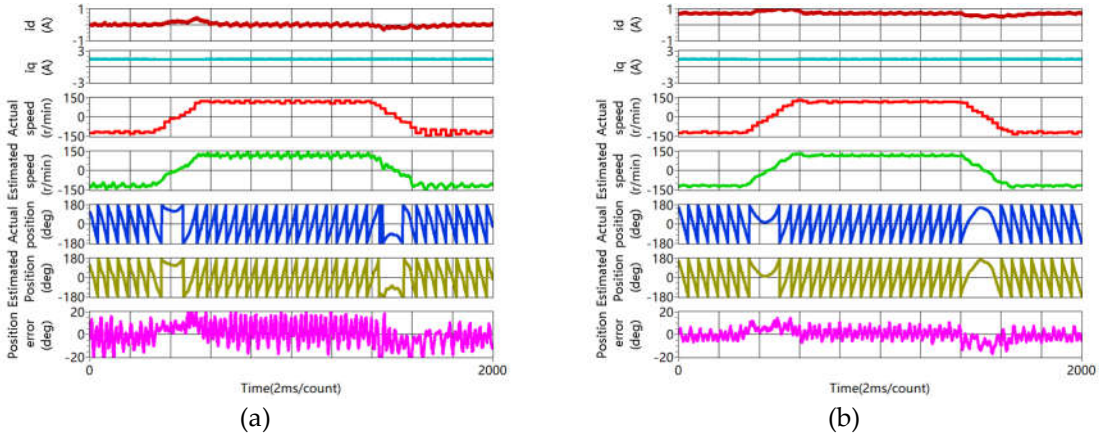

Figure 12. Rotor position estimation during the dynamic process of speed reversal test with rated load. (rotor speed changes from -120r/min to 120r/min, then back to -120r/min). (a) Conventional method; (b) Proposed method.

Figure 12 shows the experiment results during the dynamic process that speed is changed from -120r/min to 120r/min, then back to -120r/min at rated load. As shown in Figure 12a, Using the conventional $i_d = 0$ method, during the dynamic process that speed is changed to -120r/min to 120r/min, the max estimation error is greater than 20°. When the rotor speed is changed to 120r/min to -120r/min, the max estimation error is greater than -20°. However, as shown in Figure 12b, using the proposed method, the estimation error keeps within $\pm 15°$ during the speed reversal process. It proves the accuracy of rotor position estimation is enhanced using the proposed method during the speed reversal test.

Figure 13 shows the experiment results of rotor position estimation during the loading and unloading process. As shown in Figure 13a, using the conventional $i_d = 0$ method, rotor position estimation error increases with i_q during the loading process, fluctuation error is greater than $\pm 20°$

Preprints.org (www.preprints.org) | NOT PEER-REVIEWED | Posted: 27 May 2024 doi:10.20944/preprints202405.1675.v1

at 100% rated load. When the load is decreased to 0, the estimation error is around ±15°. Meanwhile, obvious fluctuation error is observed for the rotor speed estimation. However, as shown in Figure 13b, using the proposed method, the position estimation error keeps within ±10° during the dynamic loading and unloading process. When the load is decreased to 0, estimation error is less than ±5°. The speed estimation is smoother than the conventional method. So, it validates the accuracy of rotor position estimation is better using the proposed method during the loading and unloading process.

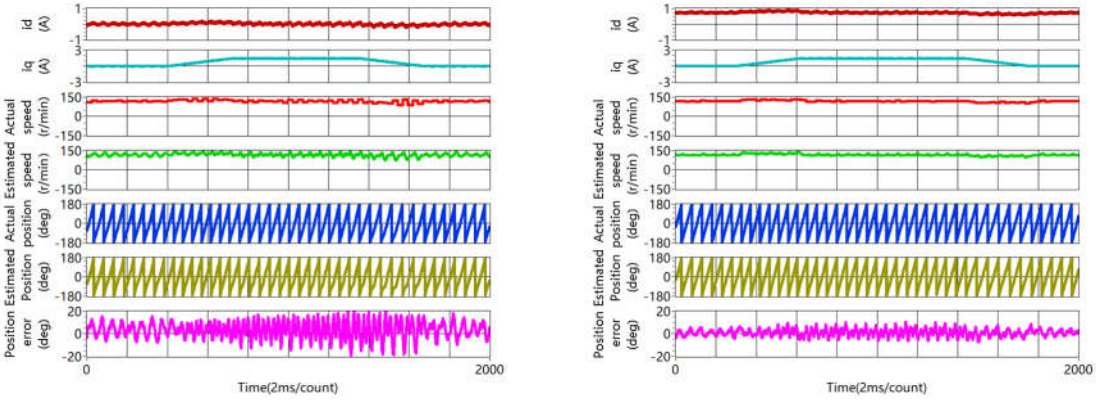

Figure 13. Rotor position estimation during the loading and unloading process at 120r/min (load is increases from 0 to rated value, then back to 0). (a)conventional method; (b)Proposed method.

Figure 14 shows the rotor position estimation when the motor is operating at 120r/min with 200% rated load. As shown in Figure 14a, Due to the effect of cross-coupling effect, almost -12° DC bias error is occurred at 200% rated load, the max position error is greater than -25°. On the contrary, As shown in Figure 14b, using the online compensation method based on parameter identification of Figure 5d, DC bias error is eliminated, the position estimation keeps around at 0°, the fluctuation error is within ±15°. The experiment data verify that the accuracy of position estimation is improved at 200% rated load.

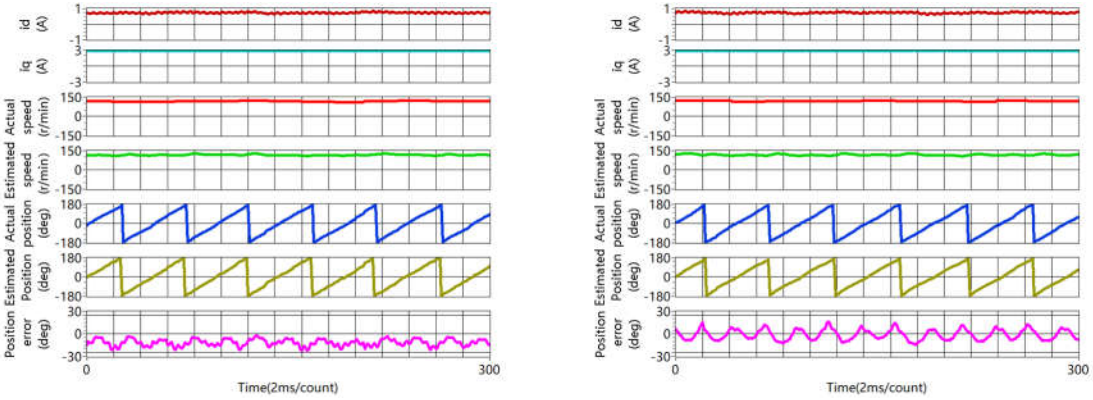

Figure 14. Rotor position estimation at 120r/min with 200% rated load. (a) Without compensation for the error due to cross-coupling effect; (b) With compensation for the error due to cross-coupling effect.

5. Conclusions

This article proposes a sensorless capability expansion method for SPMSM based on inductance parameter identification. The contribution of this article are as follows:

Preprints.org (www.preprints.org) | NOT PEER-REVIEWED | Posted: 27 May 2024 doi:10.20944/preprints202405.1675.v1

- Incremental inductances are identified by three steps combining the rotating high frequency voltage injection and pulsating high frequency voltage injection. Then, polynomial curve fitting algorithm is proposed for apparent inductances identification.
- Saliency ratio is enhanced by injecting positive DC current into *d*-axis. Comparing with the conventional $i_d = 0$ or $i_d < 0$ method, the saturation level at *d*-axis is enhanced and saliency ratio is improved obviously.
- Convergence region of pulsating high frequency voltage injection method is expanded at heavy load status. Using the conventional method, the sensorless control method fails at 120% rated current. On the contrary, using the proposed method, the rotor position estimation works well at 200% rated current.
- Experiment results show that accuracy of rotor position estimation is improved obviously at steady and during the dynamic process.

Author Contributions: Conceptualization, P.C., R.M.; methodology, Z.C.; software, P.C.; validation, Z.C.; formal analysis, P.C.; investigation, P.C., Z.C.; writing—original draft preparation, P.C., and R.M.; writing—review and editing Z.C.; visualization, Z.C.; All authors have read and agreed to the published version of the manuscript.

Funding: Please add: This work is supported by National Natural Science Foundation of China under Grant (52177059).

Data Availability Statement: The data presented in this study are available from the corresponding authors upon reasonable request.

Conflicts of Interest: The authors declare no conflicts of interest.

References

1. M. Berto, L. Alberti, V. Manzolini and S. Bolognani. Computation of Self-Sensing Capabilities of Synchronous Machines for Rotating High Frequency Voltage Injection Sensorless Control. *IEEE Trans. Ind. Electron.* **2022**, *69*, 3324–3333.
2. Y. Lee and S. -K. Sul. Model-Based Sensorless Control of an IPMSM With Enhanced Robustness Against Load Disturbances Based on Position and Speed Estimator Using a Speed Error. *IEEE Trans. Ind. Appl.* **2018**, *54*, 1448–1459.
3. M. Naderian, G. A. Markadeh, M. Karimi-Ghartemani and M. Mojiri. Improved Sensorless Control Strategy for IPMSM Using an ePLL Approach With High-Frequency Injection. *IEEE Trans. Ind. Electron.* **2024**, *71*, 2231–2241, March 2024.
4. L. Ortombina, M. Berto and L. Alberti. Sensorless Drive for Salient Synchronous Motors Based on Direct Fitting of Elliptical-Shape High-Frequency Currents. *IEEE Trans. Ind. Electron.* **2023**, *70*, 3394–3403.
5. Y. Zhang, Z. Yin, J. Liu, R. Zhang and X. Sun. IPMSM Sensorless Control Using High-Frequency Voltage Injection Method With Random Switching Frequency for Audible Noise Improvement. *IEEE Trans. Ind. Electron.* **2020**, *67*, 6019–6030.
6. Ji-Hoon Jang, S. -K. Sul, Jung-Ik Ha, K. Ide and M. Sawamura. Sensorless drive of surface-mounted permanent-magnet motor by high-frequency signal injection based on magnetic saliency. *IEEE Trans. Ind. Appl.* **2003**, *39*, 1031–1039.
7. M. Berto, L. Alberti and S. Bolognani. Measurement of the Self-Sensing Capability of Synchronous Machines for High Frequency Signal Injection Sensorless Drives. *IEEE Trans. Ind. Appl.* **2023**, *59*, 3381–3389.
8. V. Manzolini and S. Bolognani. On the Rotor Position Self-Sensing Capability of Reluctance and IPM Synchronous Motors. *IEEE Trans. Ind. Appl.* **2020**, *56*, 3755–3766.
9. T. Frenzke. Impacts of cross-saturation on sensorless control of surface permanent magnet synchronous motors. In Proceeding of the 2005 European Conference on Power Electronics and Applications. Dresden, Germany, 11-14 September 2005.
10. T. C. Lin and Z. Q. Zhu. Sensorless Operation Capability of Surface-Mounted Permanent-Magnet Machine Based on High-Frequency Signal Injection Methods. *IEEE Trans. Ind. Appl.* **2015**, *51*, 2161–2171.
11. Y. Kano and N. Matsui. Rotor Geometry Design of Saliency-Based Sensorless Controlled Distributed-Winding IPMSM for Hybrid Electric Vehicles. *IEEE Trans. Ind. Appl.* **2018**, *54*, 2336–2348.
12. J. Millinger, G. Bacco, V. Manzolini, O. Wallmark and N. Bianchi. Design and Evaluation of a Short-Circuit Rotor-Ring for Enhanced Self-Sensing Capability in a Slotless PM Motor. *IEEE Trans. Ind. Electron.* **2020**, *67*, 3462–3471.
13. P. Ponomarev, I. Petrov and J. Pyrhönen. Influence of Travelling Current Linkage Harmonics on Inductance Variation, Torque Ripple and Sensorless Capability of Tooth-Coil Permanent-Magnet Synchronous Machines. *IEEE Trans. Magn.* **2014**, *50*, 1–8.

Preprints.org (www.preprints.org) | NOT PEER-REVIEWED | Posted: 27 May 2024 doi:10.20944/preprints202405.1675.v1

14. Y. -C. Kwon, J. Lee and S. -K. Sul. Extending Operational Limit of IPMSM in Signal-Injection Sensorless Control by Manipulation of Convergence Point. *IEEE Trans. Ind. Appl.* **2019**, *55*, 1574–1586.
15. J. Lee, Y. -C. Kwon and S. -K. Sul. Signal-Injection Sensorless Control With Tilted Current Reference for Heavily Saturated IPMSMs. *IEEE Trans. Power Electron.* **2020**, *35*, 12100–12109.
16. H. Wang, K. Lu, D. Wang and F. Blaabjerg. Simple and Effective Online Position Error Compensation Method for Sensorless SPMSM Drives. *IEEE Trans. Ind. Appl.* **2020**, *56*, 1475–1484.
17. M. S. Rafaq and J. -W. Jung. A Comprehensive Review of State-of-the-Art Parameter Estimation Techniques for Permanent Magnet Synchronous Motors in Wide Speed Range. *IEEE Trans. Ind. Electron.* **2020**, *16*, 4747–4758.
18. Y. Li, Z. Q. Zhu, D. Howe, C. M. Bingham and D. A. Stone. Improved Rotor-Position Estimation by Signal Injection in Brushless AC Motors, Accounting for Cross-Coupling Magnetic Saturation. *IEEE Trans. Ind. Appl.* **2009**, *45*, 1843–1850.
19. D. Mingardi, M. Morandin, S. Bolognani and N. Bianchi. On the Proprieties of the Differential Cross-Saturation Inductance in Synchronous Machines. *IEEE Trans. Ind. Appl.* **2017**, *53*, 991–1000.
20. G. Pellegrino, B. Boazzo and T. M. Jahns. Magnetic Model Self-Identification for PM Synchronous Machine Drives. *IEEE Trans. Ind. Appl.* **2015**, *51*, 2246–2254.
21. B. Stumberger, G. Stumberger, D. Dolinar, A. Hamler and M. Trlep. Evaluation of saturation and cross-magnetization effects in interior permanent-magnet synchronous motor. *IEEE Trans. Ind. Appl.* **2003**, *39*, 1264–1271.
22. C. Wu, Y. Zhao and M. Sun. Enhancing Low-Speed Sensorless Control of PMSM Using Phase Voltage Measurements and Online Multiple Parameter Identification. *IEEE Trans. Power Electron.* **2020**, *35*, 10700–10710.
23. Q. Wang et al. An Offline Parameter Self-Learning Method Considering Inverter Nonlinearity With Zero-Axis Voltage. *IEEE Trans. Power Electron.* **2021**, *36*, 14098–14109.
24. W. Xu and R. D. Lorenz. High-Frequency Injection-Based Stator Flux Linkage and Torque Estimation for DB-DTFC Implementation on IPMSMs Considering Cross-Saturation Effects. *IEEE Trans. Ind. Appl.* **2014**, *50*, 3805–3815.
25. B. Shuang and Z. -Q. Zhu. A Novel Method for Estimating the High Frequency Incremental DQ-Axis and Cross-Coupling Inductances in Interior Permanent Magnet Synchronous Machines. *IEEE Trans. Ind. Appl.* **2021**, *57*, 4913–4923.
26. B. Shuang, Z. Q. Zhu and X. Wu. Improved Cross-coupling Effect Compensation Method for Sensorless Control of IPMSM With High Frequency Voltage Injection. *IEEE Trans. Energy Convers.* **2022**, *37*, 347–358.
27. M. Seilmeier and B. Piepenbreier. Identification of steady-state inductances of PMSM using polynomial representations of the flux surfaces. In Proceeding of IECON 2013 - 39th Annual Conference of the IEEE Industrial Electronics Society, Vienna, Austria, 10-13 Novenber 2013.
28. G. Feng, C. Lai, Y. Han and N. C. Kar. Fast Maximum Torque Per Ampere (MTPA) Angle Detection for Interior PMSMs Using Online Polynomial Curve Fitting. *IEEE Trans. Power Electron.* **2022**, *37*, 2045–2056.

Disclaimer/Publisher's Note: The statements, opinions and data contained in all publications are solely those of the individual author(s) and contributor(s) and not of MDPI and/or the editor(s). MDPI and/or the editor(s) disclaim responsibility for any injury to people or property resulting from any ideas, methods, instructions or products referred to in the content.